Research Square

Preprints are preliminary reports that have not undergone peer review.
They should not be considered conclusive, used to inform clinical practice,
or referenced by the media as validated information.

Uncertainty Analysis of Deep Learning-Based Geochemical Models Using a New Approach (Southeast Jiroft, Kerman)

Farkhondeh Khademi
University of Tehran
Dariush Esmaeily
dsmaeili@ut.ac.ir

University of Tehran
Ali Kananian
University of Tehran
Zohre Hoseinzade
Hamedan University of Technology

Article

Keywords: Maximum likelihood estimation, self-organizing neural network, deep embedded clustering, deep embedded autoencoder, recurrent neural network, geochemical anomaly, uncertainty.

Posted Date: March 3rd, 2026

DOI: https://doi.org/10.21203/rs.3.rs-8868744/v1

License: This work is licensed under a Creative Commons Attribution 4.0 International License.
Read Full License

Additional Declarations: No competing interests reported.

Uncertainty Analysis of Deep Learning-Based Geochemical Models Using a New Approach (Southeast Jiroft, Kerman)

Farkhondeh Khademi[1], Dariush Esmaeily[*1], Ali Kananian[1], Zohre Hoseinzade[2]

[1] School of Geology, College of Science, University of Tehran, Tehran, **Iran**

[2] Department of Mining Engineering, Hamedan University of Technology, Hamedan, **Iran**

*Corresponding author: Dariush Esmaeily

Email: dsmaeili@ut.ac.ir

Abstract

Identifying geochemical anomalies is key in mineral exploration and requires the application of advanced analytical methods due to the complexity of spatial data and the presence of multiple sources of uncertainty. In this study, the performance of five algorithms, including two classical methods (SOM and BSOM) and three deep learning algorithms (Embedded Autoencoder, Deep Embedded Clustering, and LSTM) was evaluated in detecting geochemical anomalies within a portion of the Urumieh-Dokhtar magmatic belt. The results indicated that each algorithm exhibits its unique performance and demonstrates relative efficiency under different conditions. Subsequently, to leverage the relative advantages of each model and reduce uncertainty, a hybrid model based on the Maximum Likelihood Estimation (MLE) method was designed and implemented. The hybrid model achieved superior performance compared to any individual algorithm by integrating the most frequent labels among the models. The validity of the obtained results was confirmed through field visits and microscopic studies of the collected samples, which revealed that valuable elements such as gold, copper, and arsenic were significantly enriched in the areas proposed by the models. Overall, the findings of this research highlight the superiority of deep learning methods, particularly the AESOM algorithm, in anomaly detection. It is recommended to use hybrid models as an effective strategy for managing exploration uncertainties.

Keywords

Maximum likelihood estimation, self-organizing neural network, deep embedded clustering, deep embedded autoencoder, recurrent neural network, geochemical anomaly, uncertainty.

Introduction

Identifying geochemical anomalies is one of the key tools in recognizing mineral indicators, as it enables the detection of areas with high mineral potential through the analysis of the chemical composition of soil, rock, and sediment samples. This method aids in detecting alteration zones, migration paths of mineralized fluids, and abnormal concentrations of metals by identifying rare or trace elements in the region [1], [2] Especially in the early stage of prospecting, geochemical investigation can predict the prospecting scope with less cost and time than other mineral prospecting means, which makes the prospecting work more targeted and precise. It can be inferred that detecting geochemical anomalies is not only important for finding mineralized zones but also represents a key activity for the definition of the spatial element and chemical compound distribution on the Earth's surface. The precise study of these anomalies through the study of dispersion patterns of trace elements, as well as the determination of migration pathways of mineralized fluids allows us to develop a unified interpretation model of genetic and tectonic processes. As a result, besides the elaboration of mineral exploration stages, for instance, those on the evolution of hydrothermal systems, prediction of alteration zones and study of the geochemical cycle can be assessed within system constraints [3], [4], [1], [5].

Thus, ensuring the accuracy and validity of data and results is a fundamental prerequisite for scientific and operational decision-making; since even the slightest uncertainty in sampling, preparation, analysis, and processing stages can lead to incorrect inferences [6], [7], [8].

However, the geochemical mapping process is inherently accompanied by a spectrum of uncertainties that can affect the accuracy, reliability, and interpretability of the results. First, the intrinsic heterogeneity of the data, resulting from the spatial dispersion of geochemical samples and the irregular sampling pattern, causes statistical and spatial estimates to not accurately represent the true subsurface conditions. Second, noise is

introduced into the data by measurement errors at the stage of field sampling or laboratory analysis, increasing the probability of erroneous interpretation of geochemical processes. Third, the accuracy of a spatial model (e.g., based on interpolation or geostatistics) in predicting values at unsampled points depends on the model's ability to capture variographic structures and regional trends. Hence, a bias will be introduced in the estimation if there is any mistake in the selection or tuning of the model [1], [8].

Complex processes such as epithermal alteration and tectonic mobilization can dictate that elements be displaced and/or concentrated, thus changing their natural distribution-patterns (an effect that, when not parameterized in the model, can lead to false anomalies or reserve underestimation). Therefore, the combination of strict quality control measures, the application of robust statistic methods that are insensitive to data outlier and the implementation of multi-scale spatial models able to capture the dynamics of geology is viewed as the baseline for minimizing uncertainty and maximizing the reliability of geochemical maps.

As a result of the aforementioned challenges, quantifying uncertainty in the geochemical anomaly identification process assumes fundamental importance; as this process provides a quantitative indicator for assessing the reliability of geochemical maps and ensures that the obtained results are scientifically and operationally dependable and applicable. Quantitative evaluation of uncertainty whether in the data collection and measurement stage or in spatial modeling and final interpretation enables the identification of error sources, estimation of potential variation ranges, and determination of confidence levels; thereby allowing evidence-based decisions grounded in risk assessment to be made [8], [9].

Therefore, uncertainty quantification is considered to be one of the key problems in spatial data analysis and geological modeling,which has also been emphasized in thedomain-specific literature [10]. The procedure of uncertainty quantification for geochemical anomaly recognition is conclusive in an increase of prediction confidence, optimization of sampling designs, and decision making, relating to exploration and environmental management. When error limits and confidence intervals are quantitatively estimated in these models, it allows researchers to deliver geochemical interpretation with higher confidence, more accurate and dependable estimates, thus reducing technical and economic risk. Furthermore, the high uncertainty areas, either caused by data sparseness and non-uniform sample distribution or geological

complexity, may be identified and used for focusing of further sampling campaign and prevents futile expenditure and redundant collections [6].

Over the past few years, a relatively extensive literature has emerged that quantifies uncertainty in the Earth sciences; or seeks to develop methods to reduce uncertainty see among others the contributions of [10], [2], [11], [12], [9], [5]. In this area, various options have been used: on one hand, the classical statistical techniques like analysis of variance, and kriging are well suited to quantify the spatial variability, and to characterize the variographic structure of the data, allowing a feasible quantification of the uncertainty [13], [14].

On the other hand, probabilistic approaches based on statistical distributions allow the uncertainty of parameters and data to be directly modeled, and can calculate the posterior distributions of geological scenarios and thus infer them opening the Bayesian-based interpretive paths. Third, several state-of-the-art machine learning and data-driven modeling techniques, such as advanced regression and neural network models, as well as random forest algorithms, have been utilized to assess uncertainty and errors in geochemical maps, and to enhance their predictive abilities [10], [13]. The synthesis of these methods gave rise to a new multidisciplinary approach to address uncertainty, enabling superior tools for geological risk analysis and resultant risk aware decisions in exploration and natural resource management.

Accordingly, this research aims to investigate and manage uncertainty in identifying geochemical anomalies by comparing the performance of classical and modern methods. To this end, five different algorithms were employed, including the Embedded Autoencoder, Deep Embedded Clustering, Long Short-Term Memory (LSTM) network, Self-Organizing Map (SOM), and its batch version (BSOM). The study area is a portion of the Urumieh-Dokhtar magmatic arc in Kerman Province, which holds potential for copper mineralization originating from fluids released from magma (epithermal/porphyry). Subsequently, to leverage the strengths of each algorithm and reduce uncertainty, a probabilistic hybrid model was designed. The evaluation of uncertainty in the applied models and the analysis of final results were validated through field visits and on-site sampling from the studied areas.

Geology of the Study Area

The study area forms part of Urumieh-Dokhtar magmatic arc. This zone lies in the southern section of the Jebal Bazez and east of the 1: 100,000 Hana map sheet (Figure 1). Within the area of investigation, a diverse Eocene to younger suite of igneous (plutonic and volcanic), volcaniclastic and sedimentary units is exposed. Andesitic lavas represent one of the most common units in this area (Fig. 2 A-B) This unit has been moderately to strongly altered. The pyroxene andesite lies also to the north of the sector. It has porphyritic and glomeroporphyritic textures. The dacitic tuff unit (gray to brown colored) crops out in the central and western portion of the land. The intrusive units in this region comprise a diverse compositional spectrum, with intrusive masses of diorite-granodiorite composition exhibiting extensive outcrops in the northern and western sections. Based on microscopic studies, the most important alterations in this unit include sericitic, argillic, propylitic, carbonatization, and iron oxide alterations (Figure 2 C-D). Another intrusive unit present in this area is monzonite, quartz monzonite, and granite. According to microscopic studies, the alterations in this unit include chloritic, argillic, carbonatization, and epidotization (Figure 2 E-F). In the northern part of the region, another intrusive unit with quartz monzodiorite composition exists. In terms of alteration, intense iron oxide alteration accompanied by intense chlorite, argillic, and phyllic alterations has occurred in this area. In parts of the area, copper mineralization in the form of malachite is observed at the impregnation level. Iron oxidation appears as limonite and hematite, and in some points, the units have undergone shearing phenomena (Figure 1) (Gohar Zamin Iron Ore Company, 2024).

Rock samples were collected from the Southeast Jiroft region, Kerman Province, southeastern Iran, as part of a collaborative study with Goharzamin Mining and Industrial Company. The company holds official exploration permits for the study area, and all samples were collected with permission and in compliance with relevant regulations.

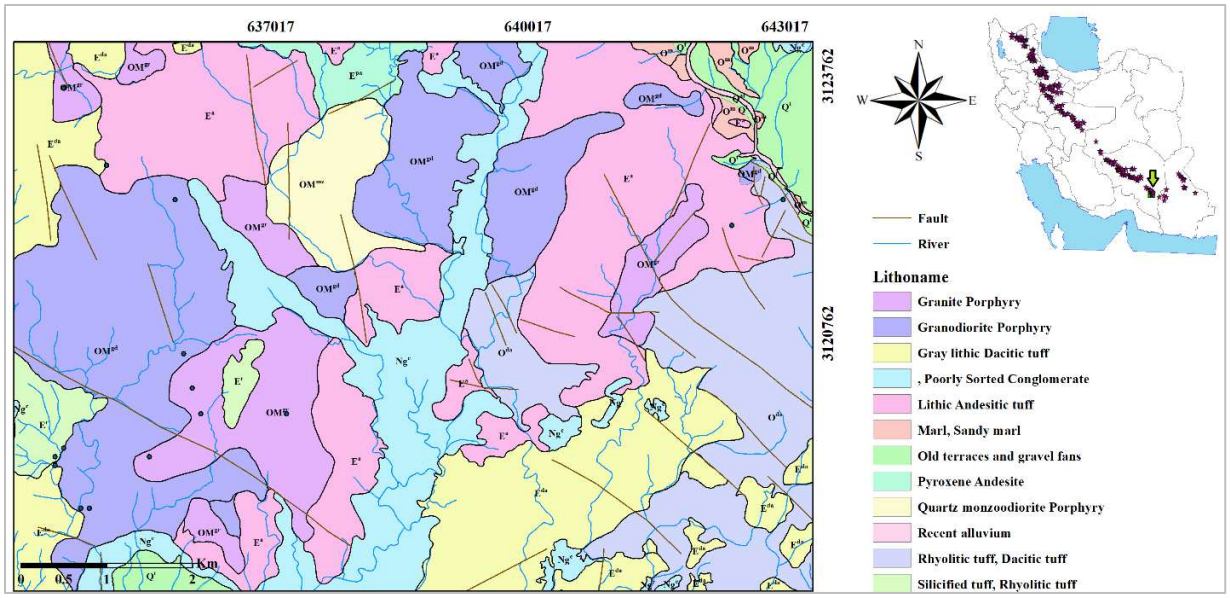


Figure 1: Geological map of the study area



Figure 2: Lithological units in the study area. A and B) Panoramic view of the campaniform andesite unit. C and D) Overview of the porphyritic granodiorite unit. E and F) Overview of the porphyritic granite unit.

Materials and Methods

Materials

In the study area, lithogeochemical data were used to produce multivariate geochemical indicators. These data were obtained from the chemical analyses of 1283 rock samples. For sample collection, a regular sampling grid with 100×100 meter cells was designed. The sampling method was systematic at 100-meter intervals. After preparing and coding the samples, they were sent to Zar Azma Company for 57-element chemical analyses. The locations of the sampling points are shown in Figure 3. The measurement method for all elements except gold is ICP-OES, and for gold, the Fire Assay preparation method is used [15].

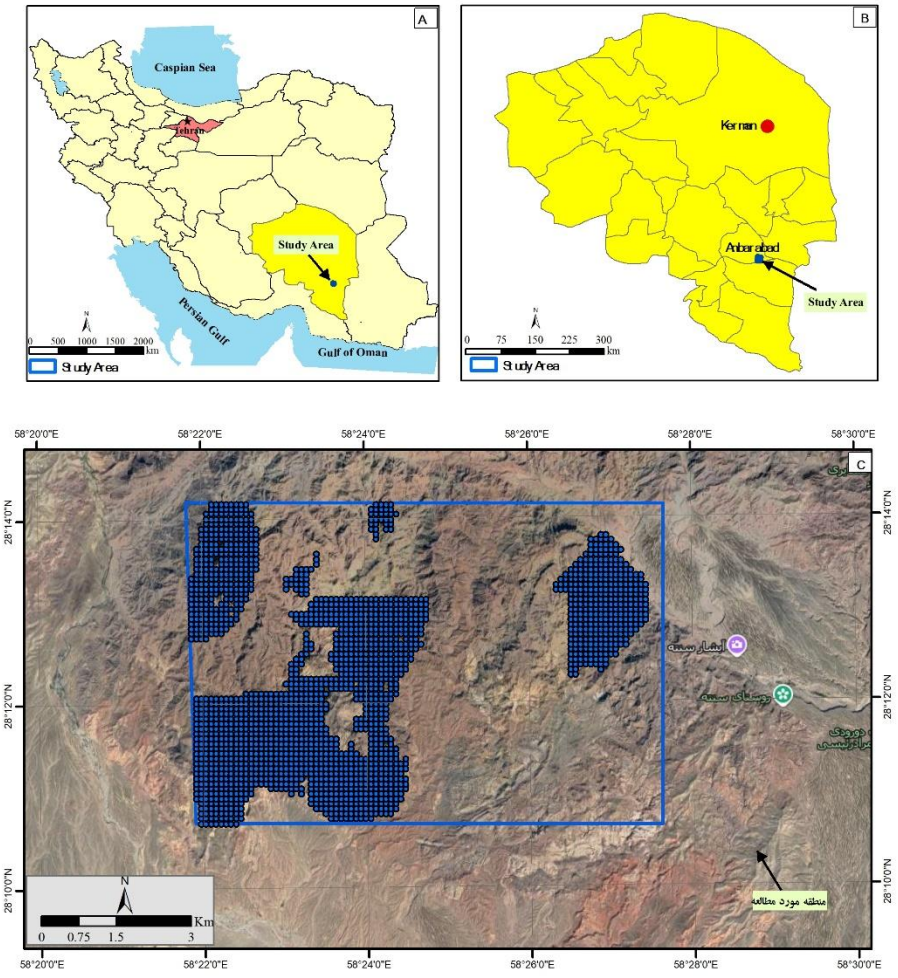


Figure 3. A) Geographic location of the study area within Iran. B) Geographic location of the study area within Kerman Province. C) Location of the collected sampling points

Methods

Self-Organizing Map

Self-organizing neural networks are recognized as an unsupervised learning approach for feature extraction and dimensionality reduction, and despite the simplicity of their implementation, they have demonstrated high performance in analyzing complex data [5].

These networks project high-dimensional data to a low-dimensional space, and at the same time, they preserve the topological properties of the original data; hence, they can be considered to be a good candidate for pattern recognition in large data. The architecture of the net is very simple, comprising only two layers: an input layer and an output layer. The output layer is commonly structured as a 2D network of neurons, where each neuron equates to a unique weight vector. The arrangement of neurons is such that their physical proximity in the output map corresponds to the neighborhood of the data in the input space [16], [17], [18].

Training proceeds like this: On presenting each input sample, the neuron, the weight vector of which is most similar to that sample, is called the winning neuron. Then the weight vector of the winning neuron and the neurons in its neighborhood are shifted towards the input sample.

This update is repeated for all training data, and over the iterations, the neighborhood radius and learning rate gradually decrease to form the final map while preserving the intrinsic structure of the data

The BSOM is a minor variation of the classical SOM algorithm and performed similarly to standard SOM in our tests (both were less effective than the deep learning models).

The main difference between BSOM and SOM is that BSOM uses batch training (updating weights after processing all data in each iteration) instead of online training (updating after each data point). This makes

BSOM faster and more stable in some cases, but in our geochemical dataset, it did not significantly improve anomaly detection compared to SOM (Figures 4).

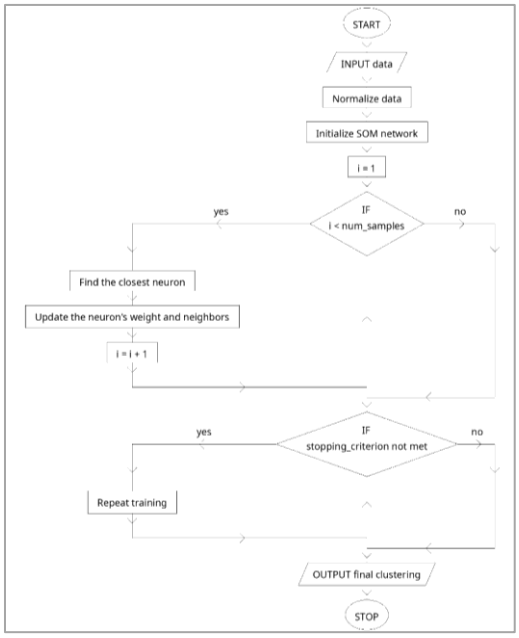


Figure 4A: Simplified flowchart of the SOM method

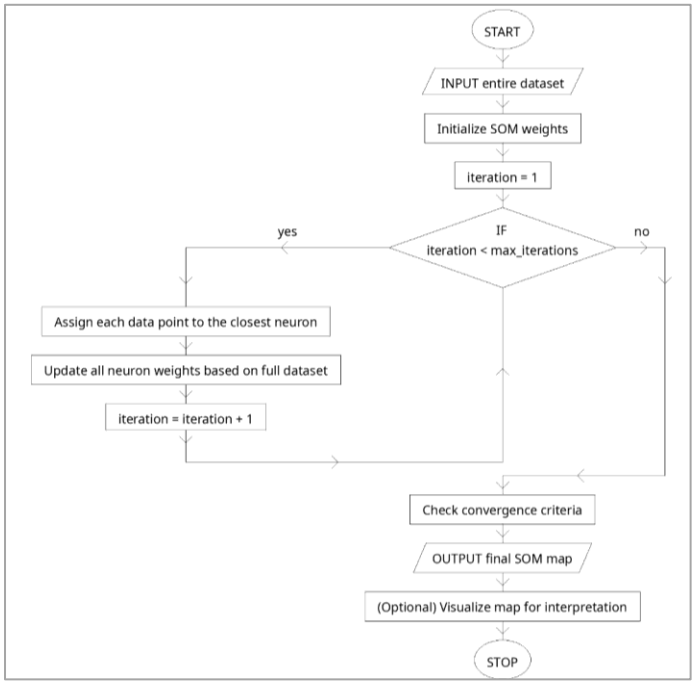


Figure 4 B: Simplified flowchart of the BSOM method

Deep Embedded Clustering

Deep Embedded Clustering is a fully unsupervised framework that, by integrating the representational capacity of deep neural networks with the precision of classical clustering algorithms, uncovers latent patterns and group structures in unlabeled high-dimensional data; this is of great importance in fields such as medical image processing, single-cell gene expression analysis, and text document clustering, which require meaningful low-dimensional representations. According to the flowchart in Figure 5, the DEC learning process consists of two sequential phases, each with its specific stages, but four main steps operate iteratively at the core of the algorithm. In the first phase, a multi-layer autoencoder is pre-trained layer-by-layer to learn a compressed representation of the data in the bottleneck layer; the network weights and initial cluster centers are initialized by running k-means on the embedded vectors, and reconstruction training continues until the error reaches a convergence threshold to form a smooth and stable space. After this pre-training, the second phase begins, in which the four steps are repeated in a cycle. First, for each embedded vector, the soft assignment probability to each cluster (q_{ij}) is calculated using the t-Student kernel to suppress the contribution of distant points. Then, the nonlinear network f_θ and cluster centers are updated by aligning this soft assignment with an auxiliary target distribution (p_i) based on minimizing the Kullback-Leibler divergence. Next, the target distribution is recalculated to increase the weight of samples that confidently belong to one cluster and to make cluster boundaries clearer. Finally, stochastic gradient descent with momentum is used to fine-tune the network parameters and the cluster centers; in the last iterations, the learning rate and momentum exponentially decrease to let the modeling converge. This four-stage cycle continues until the change in the q distribution or improvement in the loss function becomes negligible. After convergence, the embedded space arranges the samples such that points within each cluster are close to each other in a low-dimensional space, and dissimilar clusters are separated, without disrupting the topological continuity of the original data [5]. The mathematical relations for each step are presented in Figure 4, and the complete operational sequence is provided in the flowchart of Figure 5.

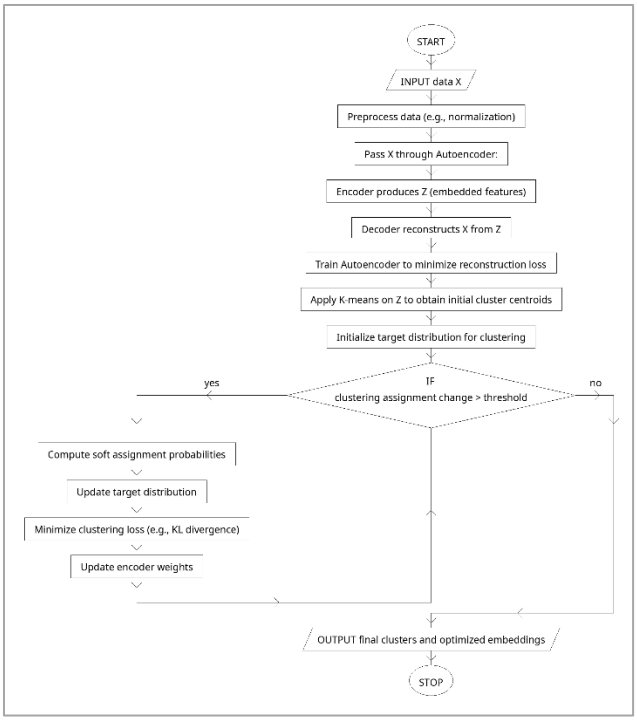


Figure 5: Simplified flowchart of the Deep Embedded Clustering method

Embedded Autoencoder

The embedded autoencoder is a type of unsupervised deep neural network that simultaneously pursues two complementary objectives: first, transforming high-dimensional and sparse input data into compact and dense representations in the bottleneck layer; second, reconstructing the same data in a way that has the least discrepancy with the original input. During training, the encoder section extracts the embedded vector z by sequentially passing the data through multiple nonlinear layers, and the decoder section, with symmetric layers, attempts to reproduce a reconstructed version of the input from z. The loss function, typically reconstruction error such as mean squared error, compels the network to store the essential information of the input in the vector z; as a result, hidden patterns become prominent, and redundant or noisy components are eliminated. These low-dimensional representations not only perform dimensionality reduction accurately but also function similarly to feature selection; since they compactly retain the principal components of the data that are vital for downstream models such as classification, regression, or clustering, and reduce computational volume. On the other hand, samples whose reconstruction is

accompanied by high error are often anomalous or noisy data, and thus the autoencoder becomes an effective tool for anomaly detection. The resulting embedded space provides a suitable foundation for clustering algorithms, since similar samples in that low-dimensional space are close to each other, and dissimilar clusters are separated from one another [19], [20], [8]. Figure 6 displays a schematic of this dual process (compression and reconstruction) and shows how the narrow central layer concentrates the complexity of the input data within itself and prepares the ground for subsequent advanced analyses.

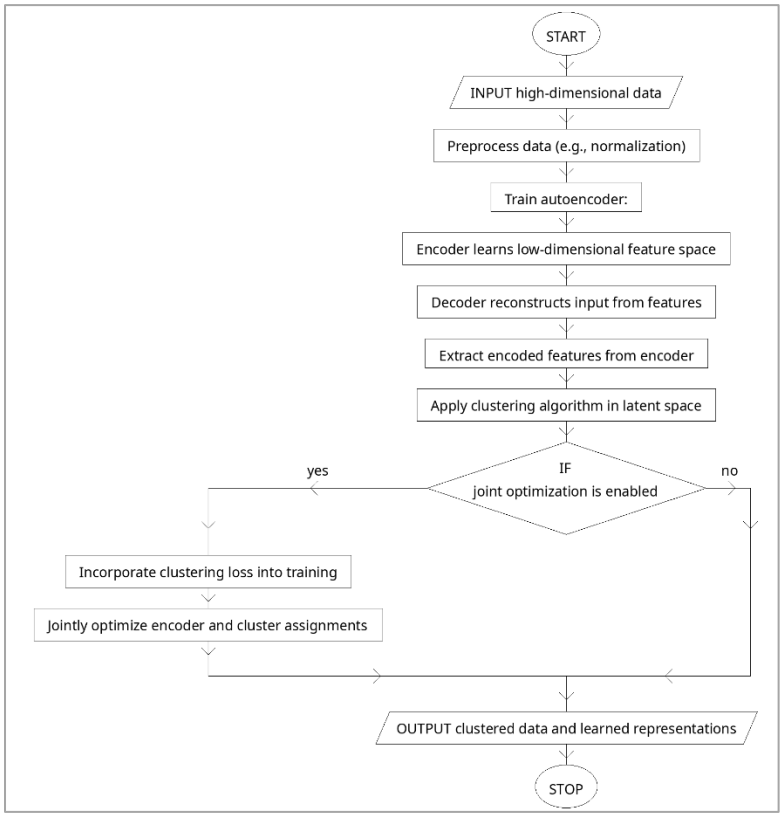


Figure 6: Simplified flowchart of the Embedded Autoencoder method

LSTM-Based Algorithm

The Long Short-Term Memory (LSTM) network is a subset of recurrent neural networks that was introduced to address the shortcomings of classical RNNs (RNNs stand for Recurrent Neural Networks. They are a type of neural network designed for sequential data, where the output from previous steps is fed back into the network to capture long-term dependencies. In our study, we used an LSTM (Long Short-Term Memory) network, which is a special

kind of RNN. LSTM solves the 'vanishing gradient' problem of classical RNNs by using memory cells and gates (forget, input, output) to remember or forget information over long sequences. We included LSTM to test if sequential patterns in geochemical data (e.g., element trends along profiles) could improve anomaly detection. It performed well, but not as well as the autoencoder-based models for our spatial dataset). in maintaining long-term dependencies in sequential data. Conventional RNNs are ineffective in transferring long-range information due to the "vanishing gradient" phenomenon; LSTM overcomes this weakness by adding a "memory cell." The memory cell acts like a conveyor belt that preserves content along the sequence and, using three regulatory gates (forgetting, input, and output), selectively decides on discarding, adding, or propagating information. The forget gate identifies components that should be discarded, the input gate incorporates valuable new information into the memory, and the output gate determines which part of the internal state is sent as the node's response to the next step; thus, the model can represent long-term relationships with greater accuracy [21]. In the next step, the features extracted by LSTM are handed over to a clustering algorithm so that observations are organized into distinct categories based on similarity. The synergy between LSTM and clustering provides a powerful framework for analyzing complex data; since not only richer indices of sequences are extracted, but hidden structures and semantic clusters are also revealed with greater clarity [22] (Figure 7).

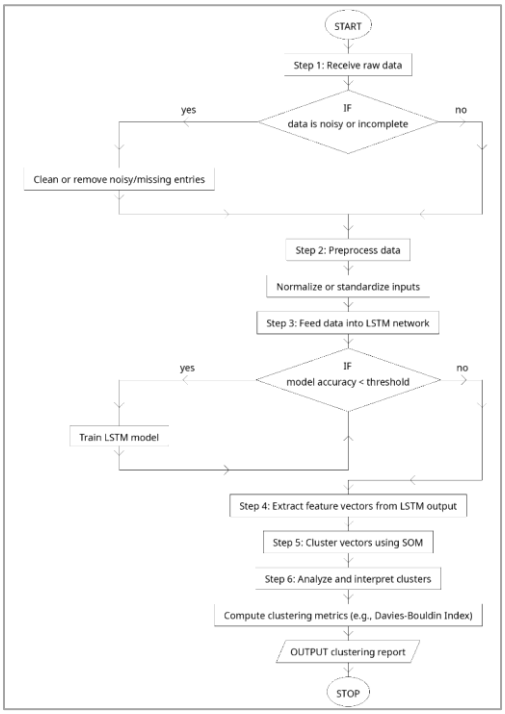


Figure 7: The streamlined flowchart of the LSTM-based technique

Preparation of Information Layers

The information layers in this study consist of 57 analyzed geochemical elements. Accordingly, in this section, geochemical maps of 12 key elements from the study area are presented (Figure 8). These are maps of the concentration of each element in bulk rock samples within the area. The elements' spatial distribution in the region is controlled by multiple factors, including geology, mineralization, alteration, and hydrothermal processes.

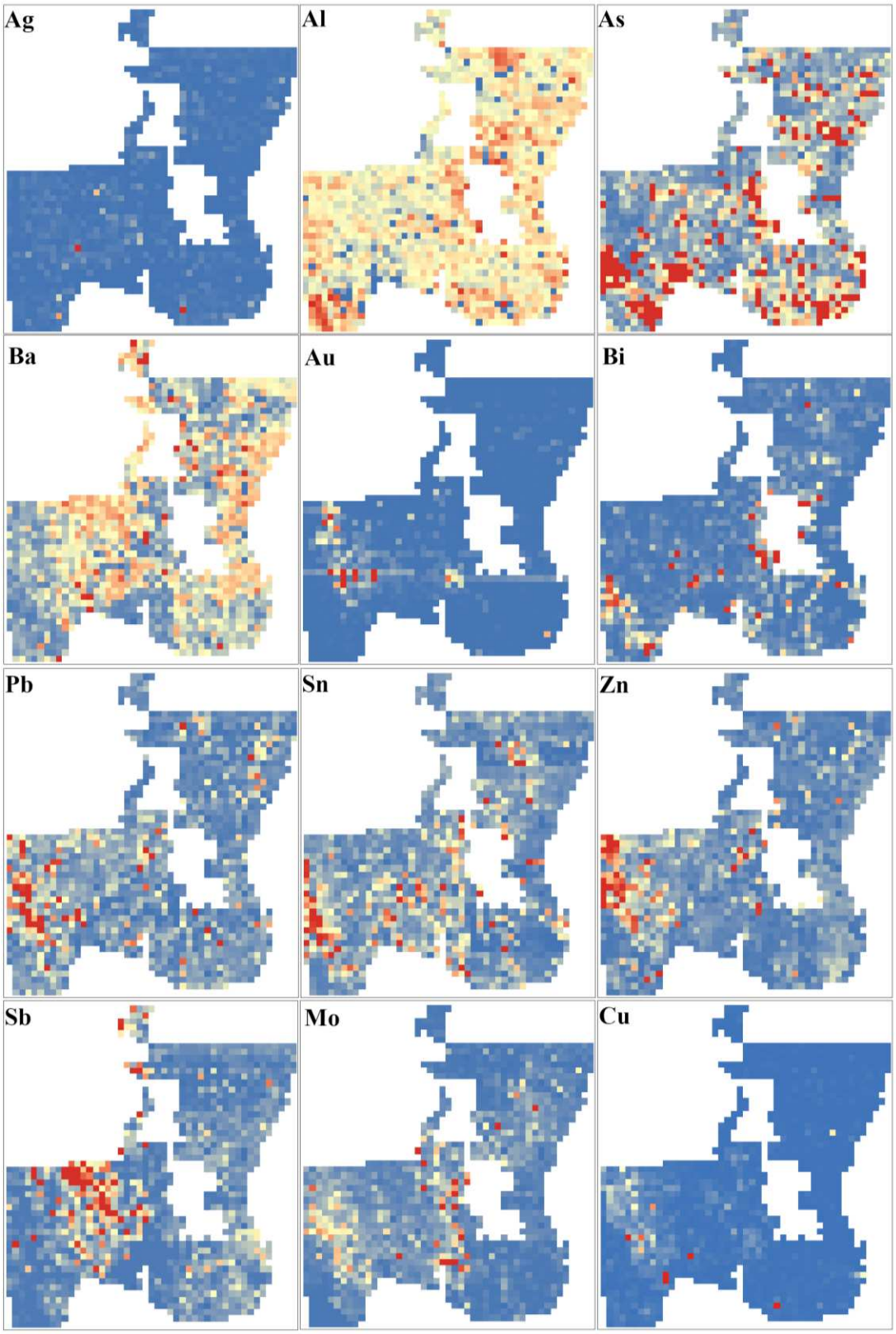

Ag
Al
As
Ba
Au
Bi
Pb
Sn
Zn
Sb
Mo
Cu

Figure 8: Concentration maps of the most relevant elements in the study area.

Discussion

In this study, to identify and delineate geochemical anomalies, three classical algorithms, including Self-Organizing Map (SOM) and Batch Self-Organizing Map (BSOM), and three deep learning-based algorithms, including Embedded Autoencoder (EAE), Deep Embedded Clustering (DEC), and Recurrent Neural Network LSTM were used. After the successful execution of the algorithms, the data were divided into 8 clusters. To determine the relative importance of the clusters, the normalized density logarithm was used as a quantitative index. This index was calculated from the ratio of the prediction rate to the percentage of the area occupied by each cluster. The mentioned criteria were extracted from the P-A plot, which was first introduced by Yousefi and Carranza in 2015. The P-A plot includes two curves that respectively display the prediction rate of known mineral occurrences and the percentage of the area covered by each class. This plot is considered a reliable criterion for evaluating geochemical models. In comparing the models, the higher the prediction rate and the lower the area percentage shown by the intersection point of the P-A curves, the higher the discrimination power and accuracy of the model in question, and consequently, it will have greater weight in the final combined model (Figure 9) ([23] [24].



Figure 9: Geochemical models produced in the study area. A) SOM B) BSOM. C) LSTM D) EAE E) DEC

Based on Table 1 and Figure 10, in the SOM model, clusters 2 and 3 have the highest weights (Log ND ≈ 1.14 and 1.07, respectively). These clusters have moderate KMO values (between 11% and 17%) and low Area (3% to 6%). In contrast, cluster 4, with a high Area (21%) and negative weight, shows signs of normality. Overall, the SOM model has not been able to sufficiently separate suspicious anomaly clusters from normal data, and the weight distribution among the clusters remains relatively balanced. In the BSOM model, cluster 1, with Weight ≈ 1.47, a high KMO (35%), and a low Area (6.7%), is highly suspicious for anomalies. Cluster 0 also has similar characteristics: KMO 23%, Area 11%, and high weight. The other clusters have very low weights. In the LSTMSOM model, cluster 5 has the highest weight (0.82) and high KMO (29%) in a moderate Area, introducing it as the main anomaly of the model. Cluster 1, with KMO 35% and weight 0.46, but in a larger Area, shows signs of a milder anomaly. The remaining clusters have weights close to zero or negative. In the DeepSOM model, cluster 2, with Weight ≈ 1.22 and a very high KMO (41%) in a moderate Area (12%), has the strongest anomaly indication. Cluster 0, with a weight 0.73 and a KMO 23%, is evaluated as suspicious. The other clusters, which have Weights and KMO close to zero, are likely normal. Overall, DECSOM has focused with high precision only on a few clusters with anomaly probability. The AEESOM model has a very strong focus on one specific anomalous cluster: cluster 2 with Weight = 1.56, KMO = 70%, and Area = 14%, clearly representing a strong anomaly. Clusters 4 and 6, with low KMO and moderate weight, may have milder anomalies. The remaining clusters have weights close to zero or negative. The overall conclusion is that AESOM has a super-focused performance and has successfully identified the anomaly in the form of one main cluster.

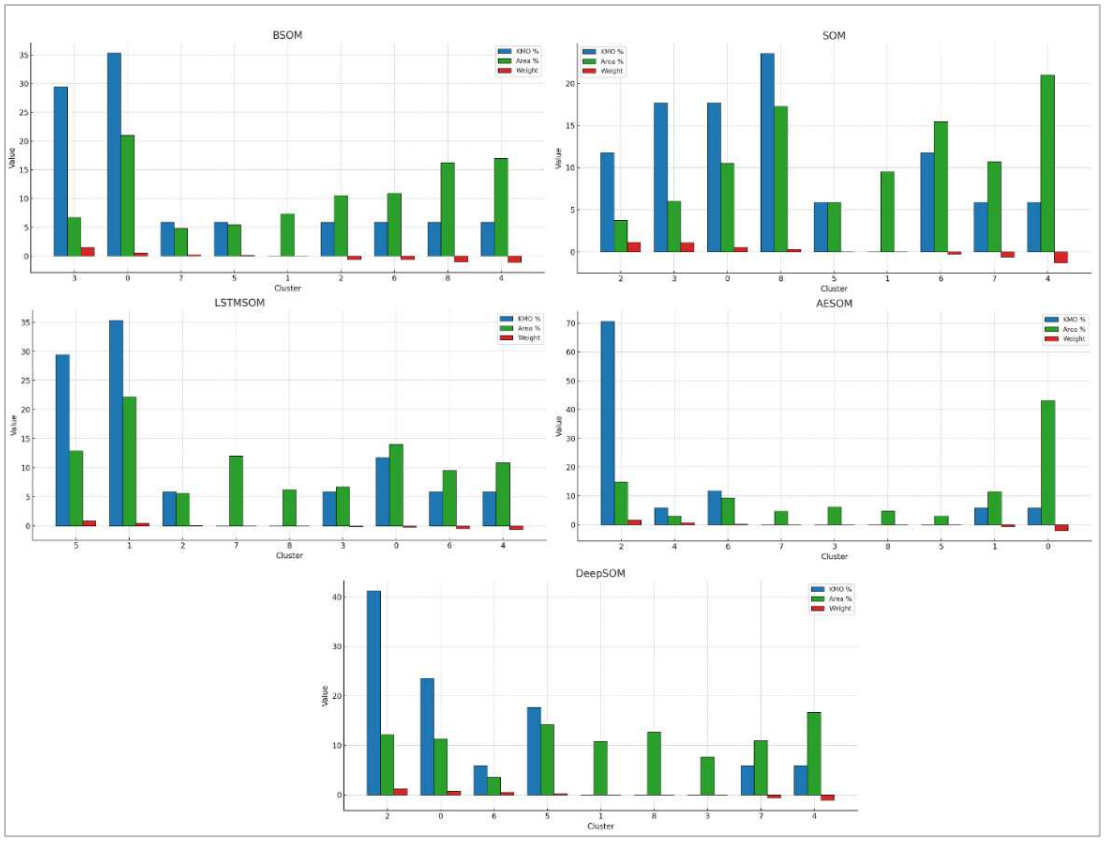


Figure 10: Bar chart of area percentage, index percentages, and cluster weights. A) SOM B) BSOM. C) LSTM D) EAE E) DEC

Table 1: Information related to the calculation of weights for different clusters.

	Cluster	KMO%	Area%	Weight		Cluster	KMO %	Area %	Weight
SOM	2	11.765	3.744	1.145	AEESOM	2	70.588	14.743	1.566
	3	17.647	6.006	1.078		4	5.882	2.886	0.712
	0	17.647	10.530	0.516		6	11.765	9.282	0.237
	8	23.529	17.239	0.311		7	0	4.680	0
	5	5.882	5.850	0.005		3	0	6.162	0
	1	0	9.516	0		8	0	4.758	0
	6	11.765	15.445	-0.272		5	0	2.964	0
	7	5.882	10.686	-0.597		1	5.882	11.466	-0.667

	4	5.882	20.983	-1.272		0	5.882	43.058	-1.991
BSOM	3	29.412	6.708	1.478	DECSOM	2	41.176	12.168	1.219
	0	35.294	20.983	0.520		0	23.529	11.310	0.733
	7	5.882	4.836	0.196		6	5.882	3.510	0.516
	5	5.882	5.460	0.074		5	17.647	14.197	0.218
	1	0	7.332	0		1	0	10.842	0
	2	5.882	10.530	-0.582		8	0	12.715	0
	6	5.882	10.920	-0.619		3	0	7.644	0
	8	5.882	16.225	-1.015		7	5.882	10.920	-0.619
	4	5.882	17.005	-1.062		4	5.882	16.693	-1.043
LSTM	0	11.760	14.040	-0.177					
	1	35.290	22.150	0.466					
	2	5.880	5.620	0.046					
	3	5.880	6.710	-0.131					
	4	5.880	10.840	-0.612					
	5	29.410	12.870	0.827					
	6	5.880	9.520	-0.481					
	7	0	12.01	0					
	8	0	6.24	0					

The individual models produced were each capable, on their own, of relatively predicting geochemical anomalies in the study area. However, the performance of the models fluctuated under different conditions, and each operated based on its own strengths. Therefore, to leverage the strengths of each model, a combined model was designed. The combination process of the models was based on the Maximum Likelihood Estimation (MLE) method. In this method, it was assumed that the final output of the combined model would be constructed based on the 5 models.

Given the lack of knowledge about the relative performance of these models and in the absence of reliable prior information, it was assumed that all models have equal validity and accuracy. As a result, the maximum likelihood approach was selected, in which the final label for each sample is determined based on the most frequent label among the model outputs. This choice, within the framework of classical probability, means maximizing the likelihood function under the assumption of independent and identically distributed data. The mentioned method, due to its simplicity, statistical interpretability, and neutrality toward the models, is considered an effective and defensible solution for combining models under uncertainty conditions. In this way, the performance of the final model was significantly improved compared to each of the models individually. This approach not only increased prediction accuracy but also enabled the analysis of the relative contribution of each model to the final decision-making. The produced combined model is presented in Figure 11, and the promising area is highlighted on it with a black frame.

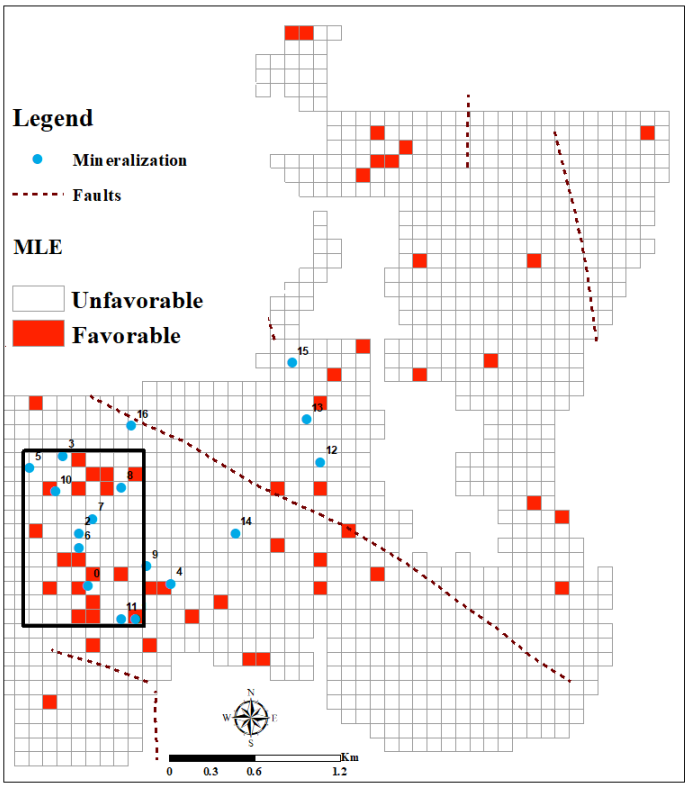


Figure 11: Map of the combined model produced based on probability.

Field Visits

Control samples were collected from promising points during field visits, which will be examined below. Sample TH-04-CH-2 was collected from the porphyritic granodiorite unit, featuring silicified veinlets and iron oxide in stockwork form. The gold concentration in this sample is 179 ppb and the copper concentration is 106 ppm, indicating enrichment of these two elements in the stockwork veinlets (Table 2 and Figure 12A). Sample TH-04-CH-3 was also collected from the porphyritic granodiorite unit, featuring silicified veinlets and copper mineralization (malachite). The gold concentration throughout in this sample is 8 ppb and the copper grade is 7526 ppm, indicating enrichment of the element in these veinlets (Table 2 and Figure 12B). Sample TH-04-CH-4 was collected from the silicified rhyolitic tuff unit, featuring silicified veinlets and copper mineralization (malachite). The gold grade in this sample is 366 ppb and the copper grade is 3770 ppm, indicating enrichment of these two elements in these veinlets (Table 2 and Figure 12C). The porphyritic granodiorite sample TH-04-CH-6 had silicified veinlets and iron oxide. The grade of gold in this sample is 172 ppb, the copper grade is 776 ppm and the arsenic grade is greater than 100 ppm, which means that these three elements have been enriched in these veinlets (Table 2 and Figure 12D). Sample TH-04-CH-7 from the porphyritic granodiorite unit also comprised silicified veinlets with iron oxide with a width of 2 meters and a length of about 10 meters.

The gold grade in this sample is 398 ppb, and the copper grade is 13172 ppm, indicating ore-grade enrichment of these two elements in these veinlets (Table 2 and Figure 12E).

Sample TH-04-CH-8 from the porphyritic granodiorite unit had silicified veins and veinlets. This sample contains gold, copper and arsenic grades of 886 ppb, 530 ppm, and over 100 ppm, which is an indication of the three elements being enriched in these veinlets (Table 2 and Figure 12F). Sample TH-04-CH-9 was taken in the dacitic lithic tuff unit, which was characterized by silicified veinlets and copper mineralization (malachite). The gold grade of this sample is 456 ppb, copper grade is 4096 ppm, and arsenic grade is more than 100 ppm, which means that there is ore-grade enrichment of these three elements in this unit (Table 2 and Figure G12). Sample TH-04-CH-10 was from the dacitic lithic tuff unit, which had silicified veinlets

and alteration. In this sample, the gold grade is 165 ppb, the copper grade is 392 ppm, and the arsenic grade is 50 ppm, and this indicates that there is enrichment of the three elements in this unit to ore-grade (Table 2 and Figure 12H). Figure 12 I-L also has clear evidence that copper mineralization has occurred in this area, with traces that had been collected in samples S-1159-M to S-9-M, and the assay results are shown in Table 2.



Figure 12: Images from field visits in the study area. A and B) Stockwork veinlets. C) Silicified veinlets along with malachite. D) Fine silicified veinlets in the rhyolitic tuff unit. E) View of the altered granodiorite unit. F) View of copper mineralization in the granodiorite unit. G) View of silicified veinlets

and iron oxide in the rhyolitic tuff unit. H) View of the altered rhyolitic tuff unit. I-J and K-L) Copper mineralization

Table 2: Assay results of samples collected in the study area. Concentration for all elements in ppm except for gold in ppb.

FID	F1	AU (ppb)	Ag	As	Cu	Mo	Sb
15	S-1159-M	17	1.2	133.33	18276	33.6	3.9
11	S-301-M	143	0.9	133.33	16015	8.8	7.4
1	S-302-M	588	0.075	133.33	2322	13.7	0.9
6	S-512-M	346	0.075	65.1	1315	38.4	0.6
2	S-553-M	567	0.9	133.33	3199	8.9	3
14	S-564-M	88	9.4	67	66666	15.3	22.2
7	S-597-M	338	0.6	30.4	1410	4.7	1
12	**S-802-M**	**136**	**2.7**	**133.33**	**-**	**14.8**	**8.2**
13	S-962-M	113	5.9	35.6	37399	3.8	2.6
10	TH-04-CH-10	165	0.3	48.9	392	5.5	11.9
8	TH-04-CH-2	179	0.075	86.9	106	2.1	5.3
16	**TH-04-CH-3**	**8**	**1.1**	**87.2**	**7526**	**2.6**	**18.1**
5	TH-04-CH-4	366	0.075	41.5	3770	10.8	2.5
9	TH-04-CH-6	172	0.9	133.33	776	31.1	5.6
4	TH-04-CH-7	398	2.9	51.8	13172	6.8	5.7
0	TH-04-CH-8	886	0.8	133.33	530	24.6	5.2

3	TH-04-CH-9	456	0.3	133.33	4096	10.6	1.6

Microscopic Studies

Selected samples were prepared for microscopic studies, some of which are presented in Figure 13. Figure 13 A, B shows sections of altered quartz monzodiorite rock that is characterized by epidotization, chloritization, sericitization, and argillic alterations. Plagioclase is the most abundant (>60%) and primary mineral observed in the sample, appearing as semi-idiomorphic to idiomorphic and tabular crystals with dimensions of 0.5 to more than 1 millimeter. Most of these crystals have undergone sericitic, argillic, and epidotic alterations. Quartz and alkali-feldspar are the other primary minerals observed in the sample, appearing as semi-idiomorphic and tabular forms with dimensions less than 1 millimeter, with an abundance close to 10%. Epidote is the most abundant secondary mineral observed in the sample, appearing as semi-idiomorphic to idiomorphic and tabular crystals with dimensions less than 1 millimeter and an abundance of more than 15% throughout all parts of the sample. Figure 13 C, D relates to porphyritic granodiorite rock with a porphyritic, poikilitic texture. Sericitic and argillic alterations are observable in this sample. The groundmass consists in most parts of semi-idiomorphic to idiomorphic and tabular crystals of quartz, plagioclase, and alkali-feldspar with dimensions less than 0.5 millimeters, and on the surface of the feldspar crystals, traces of weak sericitic alteration are also observed.

Plagioclase crystals are mainly semi-idiomorphic to idiomorphic and tabular with dimensions of 0.5 to more than 1.5 millimeters and an abundance of more than 20%, and on the surface of most of them, traces of weak sericitic and argillic alterations are observable. Quartz and alkali-feldspar crystals are also semi-idiomorphic with dimensions close to 1 millimeter and an abundance of more than 15%. Traces of weak to moderate sericitic alteration and Carlsbad twinning are also observed in the alkali-feldspar crystals.

Semi-idiomorphic sulfide minerals, which are less than 1 millimeter in dimension and less than 10% in abundance, are the secondary minerals in the rock. Figure 13 E, F is an igneous rock (most likely altered granite) with a poikilitic texture.

Its alterations are of the sericitic, argillic, and carbonatization type. Quartz, alkali-feldspar, and plagioclase with lower abundance are among the primary minerals forming this sample. Quartz and feldspar crystals are mainly semi-idiomorphic with dimensions of 0.3 to nearly 1 millimeter, showing an abundance of more than 35%. Plagioclase crystals are also semi-idiomorphic to idiomorphic and tabular with dimensions of 0.5 to more than 2 millimeters, showing an abundance of more than 40%, and most of them have undergone sericitic and argillic alterations. Thick silicified veinlets, containing semi-idiomorphic quartz crystals, crystalline carbonate molds, are also observed in parts of the thin section.

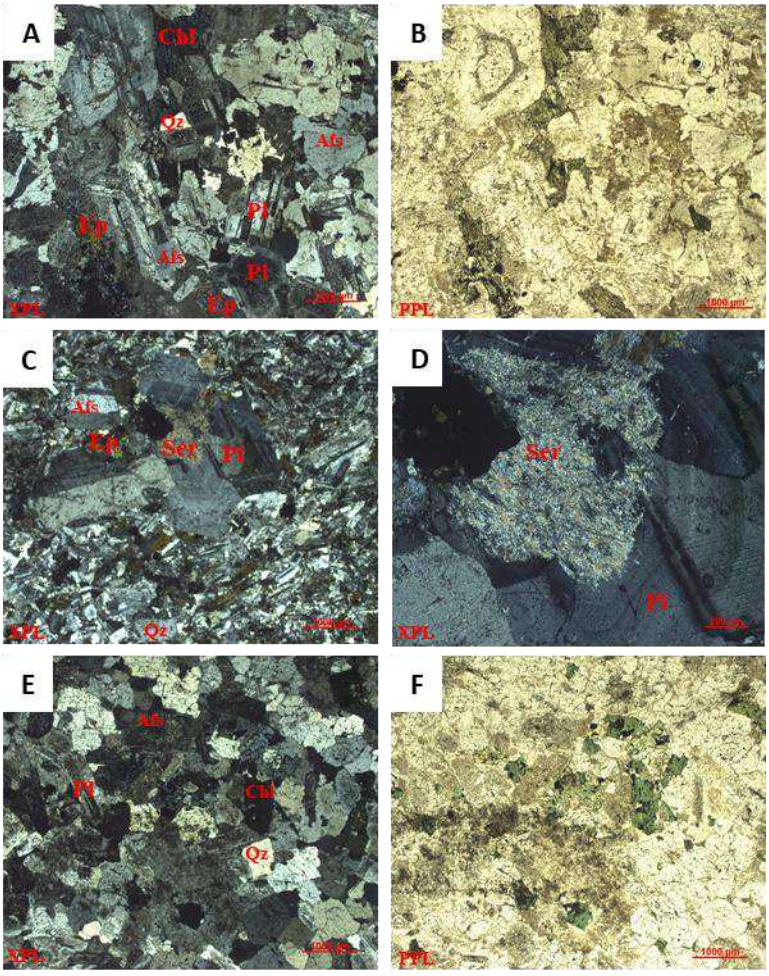


Figure 13: Microscopic images of thin sections taken from samples in the study area. A and B) Tabular plagioclase and alterations nesting in a groundmass of quartz and feldspar. C and D) Tabular quartz and

plagioclase with alterations. E and F) Sericitic and argillic altered plagioclase, thick silicified veinlet, crystalline carbonate molds.

Conclusion

In this study, the performance of five different algorithms, including two classical algorithms, SOM and BSOM, and three deep learning algorithms, Embedded Autoencoder, Deep Embedded Clustering, and LSTM, was evaluated for identifying geochemical anomalies. The results showed that each algorithm has distinct strengths and weaknesses and is capable of separating anomalous areas from normal areas in different ways. The AESOM algorithm demonstrated the highest efficiency in precisely and focally identifying anomalies and was able to provide the best performance with specific and high weighting of the anomalous cluster (Cluster 2). Additionally, the DECSOM algorithm was able to effectively separate geochemical anomalies by focusing on a limited number of clusters. In contrast, classical algorithms such as SOM and BSOM were less successful in separating anomalous clusters from normal clusters, and the cluster weighting in these models exhibited a relatively uniform distribution. Samples collected during field visits and microscopic studies confirmed the validity of the generated models. The sample assays showed these were strong areas of precious elements, including gold, copper, and arsenic, as predicted by the models. This field verification illustrates that deep learning methods, and in particular AESOM, are very accurate and robust in detecting and mapping geochemical anomalies. In general, the application of deep learning-based algorithms, in particular the AESOM model, is recommended for exploration applications. In future works, studies can led to more accurate and full results for identifying potential mineral areas by enhancing the algorithms and combining them with other exploration data.

In this research, with the aim of reducing geochemical uncertainty and enhancing the accuracy of anomaly delineation, 5 algorithms ranging from classical approaches to deep learning were employed. The two classical algorithms, SOM and BSOM, represented traditional methods, while the three deep learning-based models, AEESOM, DECSOM, and LSTMSOM, provided the capability to extract hidden nonlinear relationships in the data. The results showed that the classical SOM versions were not particularly

successful in separating anomalous clusters from normal areas; in particular, their P-A curves had intersection points with low prediction rates and relatively high areas, indicating weak discrimination power. In contrast, all three deep learning models performed better. AEESOM, relying on an embedded autoencoder and self-organizing map, assigned the highest weight (Log ND ≈ 1.56) to a main cluster and thus proved to be the most effective model in identifying enrichment anomalies of elements. DECSOM also demonstrated high discrimination by focusing on a few high-risk clusters and eliminating noise from normal clusters, although its weighting was not as concentrated as AEESOM. LSTMSOM, by leveraging sequential dependencies in the data, ranked third among the deep models in terms of Log ND index and coverage area. The close correlation of field assay results for gold, copper, and arsenic in samples TH-04-CH-2 to TH-04-CH-10 with the high-risk clusters of AEESOM and DECSOM confirmed the validity of the deep models.

The porphyritic granodiorite and rhyolitic tuff units with silicified veinlets and malachite mineralization were observed at the predicted anomalous regions. This indicates that the surface algorithms are not merely capturing statistical regularities, but also geologically meaningful signals. Clearly, there are still limitations and challenges which may be summarized as follows:

Uncertainty and variability are inherent properties of geochemical data, which may impair clustering accuracy.

Training deep learning models is a complex process, needing an appropriate data scale as well as the fine-tuning of a large number of parameters; insufficient data or overfitting will further raise the probability of making errors.

Based on this, suggestions for future research can be made:

Integration of geochemical data with geophysical, structural, and remote sensing layers within multimodal model frameworks.

Evaluation of graph neural networks (GNN) and attention-based architectures for modeling spatial dependencies.

Development of sequential validation routines, including step-by-step drilling to reduce uncertainty and adaptively adjust model weights in real-time.

Investigation of the effect of cluster size (k) and hierarchical clustering strategies on the sensitivity and specificity of anomaly maps.

In general, the results show that using AEESOM along with other deep models can significantly reduce cost and time in exploration by drilling only on targets with high probability of success. This accomplishment, by enabling decision-making based on quantitative data, will help to maximize the use of resources in exploration efforts.

Data availability: The datasets used in the current study are available from the corresponding author upon reasonable request.

Funding: This research was supported by the Iran National Science Foundation (INSF) under grant No. 4049502. The first author also received financial support from the Ministry of Science, Research and Technology (Iran) through a visiting Ph.D. fellowship.

Author Contributions Farkhondeh Khademi: Investigation, Data curation, Methodology, Funding acquisition, Formal analysis, Software, Visualization, Writing - original draft. Dariush Esmaeily: Supervision, Writing - review & editing. Ali Kananian: Supervision, Writing - review & editing. Zohre Hoseinzade: Methodology, Software, Writing - review & editing.

All authors read and approved the final manuscript.

Acknowledgements:

This research was partly supported by the Iran National Science Foundation (INSF) under grant No. 4049502. The first author also acknowledges financial support from the Ministry of Science, Research and Technology (Iran) through a visiting Ph.D. fellowship.

The authors sincerely thank Goharzamin Mining and Industrial Company for conducting the laboratory analyses of the samples and for providing logistical support, field facilities, and assistance during the fieldwork campaigns.

We gratefully acknowledge the Institute of Geotechnology and Mineral Resources, Clausthal University of Technology, Germany, for providing access to laboratory and research facilities during the research stay. We are particularly grateful to Prof. Dr. Thomas Ulrich for his valuable comments on the manuscript and for scientific discussions.

The authors also thank Dr. Mohammad Hadadi and Eng. Zakaria Pirkhazranian for their valuable assistance and cooperation throughout the project.

Competing Interests: The authors declare no competing interests. The logistical and analytical support received from Goharzamin Mining and Industrial Company did not influence the study design, data interpretation, or conclusions.

Data Availability: All data generated or analysed during this study are included in this published article and its supplementary information files.

References

[1] Z. Hoseinzade, M. H. Bazobandi, and A. R. Mokhtari, "Application of radial basis function in the analysis of irregular geochemical patterns through spectrum-area method," *J. Geochem. Explor.*, vol. 194, Nov. 2018, Art. no. 106002, doi: 10.1016/j.gexplo.2018.09.002.

[2] J. Wang and R. Zuo, "Uncertainty quantification in geochemical mapping: a review and recommendations," *Geochem. Geophys. Geosyst.*, vol. 25, no. 3, Mar. 2024, Art. no. e2023GC011301, doi: 10.1029/2023GC011301.

[3] C. Reimann, V. Melezhik, and H. Niskavaara, "Low-density regional geochemical mapping of gold and palladium highlighting the exploration potential of northernmost Europe," *Econ. Geol.*, vol. 102, no. 2, pp. 327–334, Mar. 2007, doi: 10.2113/gsecongeo.102.2.327.

[4] R. Zuo, Y. Xiong, J. Wang, and E. J. M. Carranza, "Deep learning and its application in geochemical mapping," *Earth-Sci. Rev.*, vol. 192, pp. 1–14, May 2019, doi: 10.1016/j.earscirev.2019.02.023.

[5] Z. Hoseinzade and M. H. Bazobandi, "Applying deep embedded self organizing map (DE-SOM) method to separate geochemical anomalous areas of copper-gold mineralization in Moalleman region, Iran," *J. Min. Environ.*, 2024.

[6] M. Saremi, A. Maghsoudi, A. Hezarkhani, A. B. Pour, Z. Hoseinzade, S. A. A. S. Mirzabozorg, and M. Yousefi, "Enhancing porphyry copper prospectivity mapping: a deep autoencoder-based approach to identify non-deposit points in Varzaghan region, NW Iran," *Ore Geol. Rev.*, 2025, Art. no. 106705, doi: 10.1016/j.oregeorev.2025.106705.

[7] M. Saremi, S. A. A. S. Mirzabozorg, A. Maghsoudi, M. Abedi, and R. DehghanNiri, "Cu-bearing signatures from multi-element geochemical data, a correct strategy to implement a convolutional autoencoder algorithm," *Int. J. Min. Geo-Eng.*, vol. 59, no. 1, pp. 1–10, 2025.

[8] Z. Hoseinzade and M. H. Bazobandi, “Deep embedded clustering: delineating multivariate geochemical anomalies in the Feizabad region,” *Geochemistry*, 2024, Art. no. 126208.
[9] M. Yousefi, M. D. Lindsay, and O. Kreuzer, “Mitigating uncertainties in mineral exploration targeting: majority voting and confidence index approaches in the context of an exploration information system (EIS),” *Ore Geol. Rev.*, vol. 165, Feb. 2024, Art. no. 105930, doi: 10.1016/j.oregeorev.2024.105930.
[10] J. Caers, *Modeling uncertainty in the Earth sciences*. Chichester, U.K.: John Wiley & Sons, 2011.
[11] J. Wang and R. Zuo, “Model averaging for identification of geochemical anomalies linked to mineralization,” *Ore Geol. Rev.*, vol. 146, Jul. 2022, Art. no. 104955, doi: 10.1016/j.oregeorev.2022.104955.
[12] M. Daviran, M. Parsa, A. Maghsoudi, and R. Ghezelbash, “Quantifying uncertainties linked to the diversity of mathematical frameworks in knowledge-driven mineral prospectivity mapping,” *Nat. Resour. Res.*, vol. 31, no. 5, pp. 2271–2287, Oct. 2022, doi: 10.1007/s11053-022-10164-4.
[13] P. Goovaerts, *Geostatistics for natural resources evaluation*. Oxford, U.K.: Oxford University Press, 1997.
[14] J. P. Chilès and P. Delfiner, *Geostatistics: modeling spatial uncertainty*, 2nd ed., vol. 713. Hoboken, NJ, USA: John Wiley & Sons, 2012.
[15] Gohar Zamin Iron Ore Company, “Detailed exploration study report in the area, located in the Peneh Jabal Barez,” (in Persian), Kerman, Iran, 2024.
[16] T. Kohonen, *Self-organization and associative memory*. Berlin, Germany: Springer-Verlag, 1984.
[17] T. Kohonen, “The self-organizing map,” *Proc. IEEE*, vol. 78, no. 9, pp. 1464–1480, Sep. 1990, doi: 10.1109/5.58325.
[18] T. Kohonen, “Exploration of very large databases by self-organizing maps,” in *Proc. Int. Conf. Neural Networks*, 1997, pp. PL1–PL6.
[19] A. Boubekki, M. Kampffmeyer, U. Brefeld, and R. Jenssen, “Joint optimization of an autoencoder for clustering and embedding,” *Mach. Learn.*, vol. 110, no. 7, pp. 1923–1953, Jul. 2021, doi: 10.1007/s10994-021-06015-5.
[20] P. Li, Y. Pei, and J. Li, “A comprehensive survey on design and application of autoencoder in deep learning,” *Appl. Soft Comput.*, vol. 138, May 2023, Art. no. 110176, doi: 10.1016/j.asoc.2023.110176.
[21] A. Sherstinsky, “Fundamentals of recurrent neural network (RNN) and long short-term memory (LSTM) network,” *Physica D*, vol. 404, Mar. 2020, Art. no. 132306, doi: 10.1016/j.physd.2019.132306.
[22] J. Wang and R. Zuo, “Identification of geochemical anomalies through combined sequential Gaussian simulation and grid-based local singularity analysis,” *Comput. Geosci.*, vol. 118, pp. 52–64, Sep. 2018, doi: 10.1016/j.cageo.2018.05.010.
[23] M. Mokhtari, Z. Hoseinzade, and K. Shirani, “A comparison study on landslide prediction through FAHP and Dempster–Shafer methods and their evaluation by P–A plots,” *Environmental Earth Sciences*, vol. 79, no. 3, Jan. 2020, Art. no. 39, doi: 10.1007/s12665-019-8804-0.
[24] Z. Hoseinzade, A. Zavarei, and K. Shirani, “Application of prediction-area plot in the assessment of MCDM methods through VIKOR, PROMETHEE II, and permutation,” *Natural Hazards*, vol. 109, no. 3, pp. 2489–2507, 2021, doi: 10.1007/s11069-021-04929-w.